

# Mechanism of Na-Ion Storage in Hard Carbon Anodes Revealed by Heteroatom Doping

Zhifei Li, Clement Bommier, Zhi Sen Chong, Zelang Jian, Todd Wesley Surta, Xingfeng Wang, Zhenyu Xing, Joerg C. Neufeind, William F. Stickle, Michelle Dolgos,\* P. Alex Greaney,\* and Xiulei Ji\*

Hard carbon is the leading candidate anode for commercialization of Na-ion batteries. Hard carbon has a unique local atomic structure, which is composed of nanodomains of layered rumpled sheets that have short-range local order resembling graphene within each layer, but complete disorder along the *c*-axis between layers. A primary challenge holding back the development of Na-ion batteries is that a complete understanding of the structure–capacity correlations of Na-ion storage in hard carbon has remained elusive. This article presents two key discoveries: first, the characteristics of hard carbon structure can be modified systematically by heteroatom doping, and second, that these structural changes greatly affect Na-ion storage properties, which reveals the mechanisms for Na storage in hard carbon. Specifically, via P or S doping, the interlayer spacing is dilated, which extends the low-voltage plateau capacity, while increasing the defect concentrations with P or B doping leads to higher sloping sodiation capacity. The combined experimental studies and first principles calculations reveal that it is the Na-ion-defect binding that corresponds to the sloping capacity, while the Na intercalation between graphenic layers causes the low-potential plateau capacity. The understanding suggests a new design principle of hard carbon anode: more reversibly binding defects and dilated turbostratic domains, given that the specific surface area is maintained low.

## 1. Introduction

Na-ion batteries (NIBs) represent one of the most promising solutions for grid-scale storage of electrical energy produced by intermittent renewable energy sources, such as wind and solar power. Their potential for massive scale-up is high because they are electrochemically similar to Li-ion batteries (LIBs), but unlike LIBs can be composed entirely of inexpensive and earth-abundant elements. Cathode materials, including layered oxides and polyanion compounds, have exhibited very promising performance for NIBs.<sup>[1]</sup> Unfortunately the principal anode materials for LIBs, graphite, only stores sodium up to a stoichiometry of NaC<sub>64</sub>, one-tenth of its capacity for lithium storage unless graphite is expanded or solvent co-intercalation occurs,<sup>[2]</sup> and so alternative anode materials are being sought. These candidate materials, in addition to having high sodium capacity, must also meet the requirements for scale-up by being inexpensive to produce in large quantities with minimal environmental impact.

Currently the most promising candidate is an allotrope of carbon called hard carbon (HC). This is an amorphous form of turbostratic carbon comprising nanoscale domains of stacked, rumpled graphenic sheets.<sup>[3]</sup> Within each plane, the sheets have graphene-like order, but the sheets lack long-range ordering and are therefore disordered along the *c*-axis. The titular adjective “hard” refers to the materials reluctance to transform to graphite during annealing and its sp<sup>3</sup> carbon atoms contained, and as such it is also known as nongraphitizable carbon. The ability of hard carbon to accommodate a large quantity of Na-ions electrochemically was first demonstrated by Stevens and Dahn in 2000.<sup>[4]</sup> Since then, a worldwide research effort has enhanced its storage capacity, and advanced numerous processes for synthesizing hard carbon from abundant feed stocks, such as sucrose,<sup>[5]</sup> peat moss,<sup>[6]</sup> cotton,<sup>[7]</sup> wood,<sup>[8]</sup> and banana skins.<sup>[9]</sup> Most of this advancement has been Edisonian in nature, because efforts to attribute features of the sodiation profile to hard carbon structure have not fully appreciated the subtlety of its structure. That hard carbon does not readily

Z. Li, Dr. C. Bommier, Z. S. Chong, Dr. Z. Jian, T. W. Surta, X. Wang, Dr. Z. Xing, Prof. M. Dolgos, Prof. X. Ji  
Department of Chemistry  
Oregon State University  
Corvallis, OR 97331-4003, USA  
E-mail: michelle.dolgos@oregonstate.edu; david.ji@oregonstate.edu

Dr. J. C. Neufeind  
Chemical and Engineering Materials Division  
Oak Ridge National Laboratory  
Oak Ridge, TN 37831, USA

Dr. W. F. Stickle  
Hewlett-Packard Co.  
1000 NE Circle Blvd., Corvallis, OR 97330, USA

Prof. P. A. Greaney  
Materials Science and Engineering  
University of California  
Riverside, 900 University Ave., Riverside, CA 92521, USA  
E-mail: agreaney@engr.ucr.edu

DOI: 10.1002/aenm.201602894

transform to graphite indicates that, unlike other amorphous (nongraphitic) carbons, its graphenic sheets possess a topology that cannot be unfolded and flattened—topology that is also beneficial for Na storage.

Early work proposed a Na-ion storage mechanism that followed that for Li, where storage during the sloping region in the sodiation profile is attributed to intercalation of Na-ions into turbostratic nanodomains, and the capacity from the low-potential plateau is attributed to nanoplating (adsorption) inside the “enclosed” micropores between the domains. Our recent studies lead us to propose an alternative model. We annealed hard carbon at high temperatures, with the aim that the resulting increased size of turbostratic nanodomains would increase the capacity under the sloping region of the sodiation profiles.<sup>[10]</sup> Instead we found the reverse trend, that the capacity of the sloping region was reduced. This contradiction suggests an alternative correlation, where the removal of defects by annealing results in the decrease of sloping capacity, and thus we tentatively attribute the sloping capacity to favorable binding of Na at local defects rather than indiscriminate Na-ion intercalation. Other experiments have also led us to question which Na storage sites are filled during the plateau region of the sodiation profile. X-ray diffraction measurements of the (002) *d*-spacing (the average intersheet spacing) indicate marked dilation between sheets during the low-potential plateau sodiation, which suggests that the plateau capacity might originate from intersheet intercalation of Na-ions instead of nanoplating in micropores.<sup>[6,11]</sup> One can test this hypothesis by determining whether a higher capacity is obtained by a hard carbon with a larger initial (002) *d*-spacing between the graphene sheets inside turbostratic nanodomains. It is reasonable to hypothesize that a larger initial sheet spacing incurs a lower strain energy penalty for Na-ion intercalation. Recently, Huang and co-workers and Jiang and co-workers investigated heteroatom doping into carbon structures, where the authors report that doping facilitates a larger *d*-spacing, which is responsible for the higher capacity.<sup>[12]</sup> It is important to note that these reported carbons are not conventional hard carbon known by the field as they were pyrolyzed at relatively low temperatures, and therefore do not exhibit a low-potential plateau behavior.

A straightforward empirical approach to reveal storage mechanisms is to enhance the hypothesized desirable local structures of hard carbon and monitor the corresponding capacity variation. One of the most promising methods for engineering the structure of hard carbon is through heteroatom doping, and to date, many dopants have been investigated for various hard carbon materials.<sup>[12a,13]</sup> However, thus far there has been no systematic knowledge of how doping affects the local structure of hard carbon, and the carbon materials reported in the literature vary hugely in their specific surface areas. This makes it difficult to compare carbon structures because in materials with large surface area the formation of solid electrolyte interphase (SEI) can mask the reversible capacity from the internal local structures.<sup>[14]</sup>

In this article, we elucidate the structure–capacity correlation for hard carbon with a systematic set of experiments that address the challenges above using controlled syntheses combined with detailed structural and electrochemical characterization, as well as first principles density functional theory (DFT)

calculations of Na-ion binding energetics with representative structural sites. The work is presented in two parts. The first demonstrates that we have used boron, phosphorous, and sulfur doping to tune two different structural characteristics of turbostratic nanodomains: the interlayer spacing and the defect concentration. The second part of the article presents detailed electrochemical characterization of these materials and computational analysis of probable Na storage sites.

We have prepared “conventional” hard carbons by pyrolysis of sucrose at 1100 °C, and all hard carbon samples in this study are of consistently low specific surface areas, that is <10 m<sup>2</sup> g<sup>-1</sup>, enabled by our well-established method.<sup>[5,15]</sup> Recently, we reported that P-doped hard carbon exhibits a record-high reversible desodiation capacity of 359 mA h g<sup>-1</sup> at 20 mA g<sup>-1</sup>; though a hypothesis of favorable structural sites is raised, the structure–capacity correlation is not solidified.<sup>[5]</sup> In this study, we introduce two more doped hard carbon materials: B-doped and S-doped, in addition to the P-doped hard carbon. B-doping was used to increase the number of in-plane local defects because boron can only form three bonds in the absence of strong Lewis bases, thus B-doping more likely takes place within the graphenic planes. It is either the doped-B atoms or doping-induced carbon vacancies that will serve for the more enhanced presence of in-plane defects. Note that a computational study suggested that boron-doping can improve the performance of graphene as an anode in NIBs.<sup>[16]</sup> We selected doping phosphorus and sulfur to increase the interlayer spacing between graphene sheets by steric occupancy. We used boric acid, phosphoric acid, and sulfuric acid as precursors because the respective oxo-acids can be mixed with carbon precursor sucrose in a molecular level, which ensures the near-atomic dispersion of the dopants.

Synthesis of these materials was followed by detailed structural and chemical characterization using X-ray diffraction (XRD), Raman spectroscopy, neutron total scattering, and transition electron microscopy (TEM) equipped with energy-dispersive X-ray mapping (EDX). Together these provided a picture of the doped hard carbons mesoscale structure, chemical structure, and short- and intermediate-range atomic order. It was revealed that both P- and B-doping that bring more defects produce significantly enlarged Na-storage capacity in the first sodiation sloping region of the potential profiles. Both S- and P-doping increase the interlayer spacing between graphenic sheets and have increased Na-storage capacity in low-potential plateau region. Our computation results further confirm that P- and B-doped sites, as well as carbon vacancies, bind with inserted Na-ions much more strongly than a defect-free graphene sheet, resulting in relatively high sodiation potentials—typically seen on the sloping region. Our results provide solid evidence that supports our hypothesis of structure–capacity correlation, where the low-potential plateau is attributed to the Na-ion binding on low-energy sites, most likely inside turbostratic nanodomains and the sloping region corresponds to the Na-ion binding on high-energy defective sites. We also find that the large first sodiation capacity of B-doped hard carbon is highly irreversible in the following desodiation process. Our combined experimental and first principles studies reveal that it is the high binding energy between the in-plane B-dopants and Na-ions that cause the irreversibility. This raises a new trapping

mechanism that has nothing to do with SEI and an associated corresponding design principle, where one should avoid introducing high-energy defects inside turbostratic nanodomains.

## 2. Results and Discussion

### 2.1. Structure Characterization of Synthesized Materials

All the dopant precursors are soluble in the sucrose aqueous solution; this helps achieve the atomic dispersion of dopants in the final products, as demonstrated in our previous work.<sup>[5]</sup> We aim at 5 wt% of doping by assuming that the dopants are not volatile and the yield of sucrose carbonization is 25 wt%. We determined the doping levels by inductively coupled plasma optical emission spectrometry (ICP-OES) to be 3.0, 3.0, and 0.1 wt% for P-doped (P-HC), B-doped (B-HC), and S-doped (S-HC) hard carbon, respectively. Note that the S-doping level is significantly lower than the target amount of doping because sulfuric acid is most likely reduced into SO<sub>2</sub> gas during pyrolysis. Near-atomic level distribution of dopant was achieved, as shown in P-HC in our previous work.<sup>[5]</sup> The densities for all carbons were measured based on Archimedes' principle, which are 1.60, 1.42, 1.50, and 1.49 g cm<sup>-3</sup> for nondoped HC, P-HC, B-HC, and S-HC, respectively. The much lower densities of all these carbons compared to graphite (2.11 g cm<sup>-3</sup>, our measured value) indicate larger *d*-spacing between graphenic layers or enclosed nanovoids in the structures.<sup>[17]</sup> All as-obtained HC, P-HC, B-HC, and S-HC exhibit very low Brunauer–Emmett–Teller (BET) surface area of 8.5, 7.3, 8.0, and 5.2 m<sup>2</sup> g<sup>-1</sup>, respectively. All these carbons consist of bulk particles, tens of micrometers large, as shown in the scanning electron microscope (SEM) images (Figure S1, Supporting Information). The consistently low surface area and similar morphology of these carbons will facilitate a faithful comparison between their local structures and the corresponding electrochemical performance. Importantly, by pyrolysis treatment at 1100 °C, these carbon samples belong to the category of “conventional” hard carbon so that the mechanistic insights obtained on them can be employed to explain phenomena of the most hard carbon materials in the literature.

We investigated the oxidation states of the dopants by X-ray photoelectron spectroscopy (XPS) (Figure S2, Supporting Information). None of the dopants became fully reduced to its elemental valance from their oxo-acid precursors. Phosphorus in P-HC occurs in P(V), P(II), and P–C bonds with its 2p signal deconvoluted into components at 134.5, 133.1, and 131.0 eV, respectively (Figure S2a, Supporting Information).<sup>[18]</sup> As for S-HC, the sulfur 2p signal is deconvoluted into peaks at 168.3, 164.9, and 163.9 eV, attributed to C–SO<sub>x</sub>, S 2p<sub>1/2</sub>, and S 2p<sub>3/2</sub> of C–S–C, respectively (Figure S2b, Supporting Information).<sup>[12a,19]</sup> For B-HC, boron may occur in the doped sample in boron oxides, BCO<sub>2</sub>, BC<sub>2</sub>O, and B<sub>3</sub>C, as suggested by deconvoluted B<sub>1s</sub> peaks at 193.3, 192.5, 191.6, and 190.8 eV, respectively (Figure S2c, Supporting Information).<sup>[20]</sup>

The X-ray diffraction (XRD) results reveal the nongraphitic structure of carbons and confirm our hypothesis that P- and S-doping would increase the average interlayer *d*-spacing, whereas the interlayer distance of B-HC stays nearly the same.

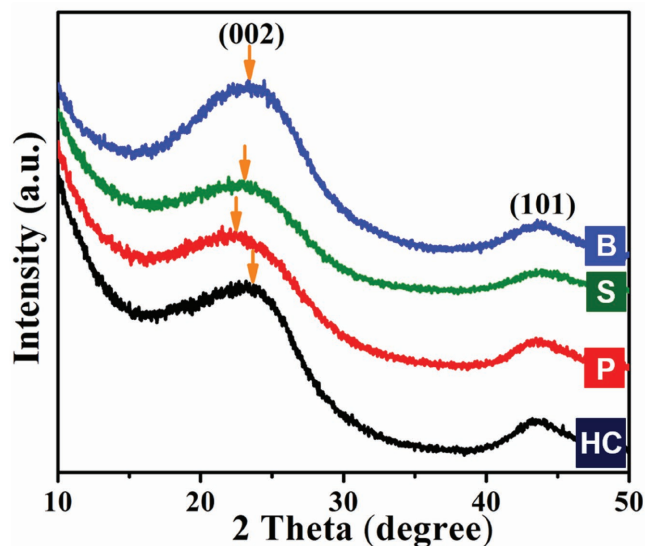


**Figure 1.** XRD patterns of doped and undoped carbons. After P- and S-doping, the (002) peak shifts to a lower angle, which indicates a larger *d*-spacing. However, B-doping barely shifts the peak.

The positions of (002) peaks determined by the PDXL software are at 23.6°, 22.5°, 23.2°, and 23.5°, indicating *d*-spacing values of 3.77, 3.95, 3.83, and 3.78 Å for HC, P-HC, S-HC, and B-HC, respectively (Figure 1). The error bar for these *d*-spacing values is  $\approx \pm 0.01$  Å, related to the measurement setup. High-resolution TEM images demonstrate typical hard carbon turbostratic structures, as shown in Figure 2. It seems that graphenic layers in P-HC are more curved than those in HC, while some graphenic layers in B-HC are longer and less curved than HC.

Raman spectra can estimate the coherence lengths of graphenic domains along lateral *ab* direction (*L<sub>a</sub>*) according to the following equation

$$L_a \text{ (nm)} = (2.4 \times 10^{-10}) \lambda_{nm}^4 \left( \frac{I_G}{I_D} \right) \quad (1)$$

where  $\lambda_{nm}$  is the laser wavelength: 514 nm, and *I<sub>G</sub>* and *I<sub>D</sub>* are intensity of the G band and D band, respectively.<sup>[21]</sup> The D band at  $\approx 1350$  cm<sup>-1</sup> is attributed to the A<sub>1g</sub> phonons of the breathing mode of C<sub>6</sub> rings activated by the existence of defects, while the G band at  $\approx 1600$  cm<sup>-1</sup> corresponds to the E<sub>2g</sub> vibration of the sp<sup>2</sup> carbon atoms. To identify D and G bands accurately, two broad peaks in Raman spectra are deconvoluted into four Lorentzian peaks, as shown in Figure 3. With the above equation, HC, P-HC, S-HC, and B-HC exhibit *L<sub>a</sub>* values of 12.9, 12.1, 14.2, and 14.6 nm. P-HC exhibits the shortest coherence length of *L<sub>a</sub>*, which indicates that graphenic layers in P-HC may be shorter or more curved, where the latter scenario is supported by TEM imaging. Furthermore, the Raman results indicate that B-HC has the largest average domain size of graphenic layers, which corroborates the TEM results.

It was extremely challenging to fully understand the local structures of amorphous carbon by conventional characterizations. Fortunately, recently, tremendous progress has been made with pair distribution function (PDF) studies associated with high-energy X-ray and neutron total scattering, which can

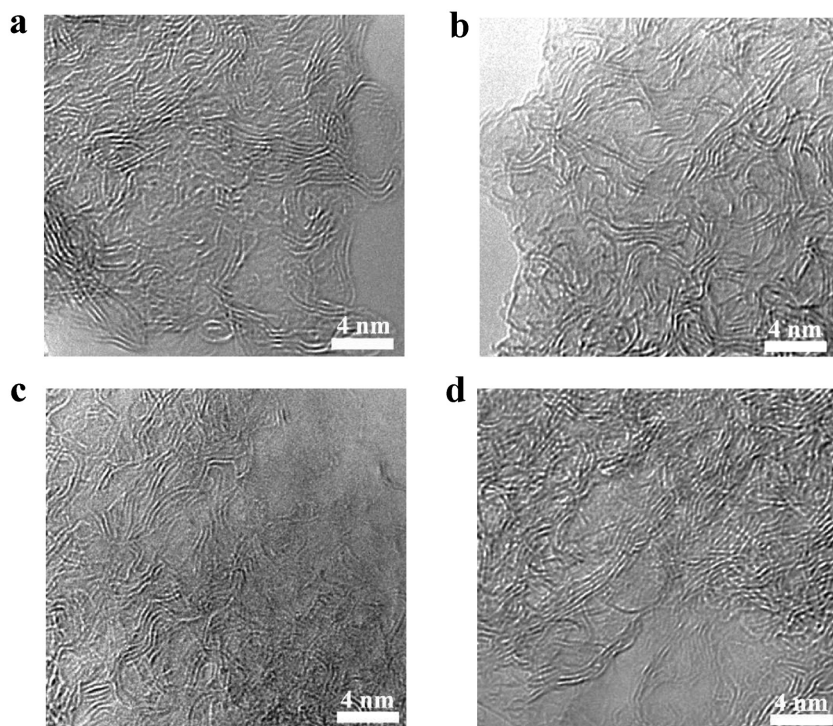


**Figure 2.** TEM images of carbon samples. a) HC, b) P-HC, c) S-HC, and d) B-HC. All carbons demonstrate a nongraphitic structure comprising curved graphenic layers, where the lines are from the edge-view of the graphenic layers. Despite that the images are taken from a small scale of dimensions, it appears that P-doping facilitates more curvature in the hard carbon.

help reveal the local structures of nanomaterials and amorphous carbon.<sup>[22]</sup> In our prior studies, we determined local defect levels by neutron total scattering and PDF studies, where defects are correlated to the sloping region of potential profiles.<sup>[5,10]</sup> To obtain the PDF results, a Fourier transform of the structure function  $S(Q)$  is carried out with the following equation

$$\frac{A}{4\pi} G(r) = A\rho[g(r) - 1] \\ = \frac{1}{2\pi^2} \sum_0^{Q_{\max}} QA[s(Q) - 1] \sin(QR)\Delta Q \quad (2)$$

where  $Q$  is the scattering vector,  $\rho$  is the atomic number density,  $g(r)$  is the atomic pair distribution function, and  $A$  is a constant generated during normalization.<sup>[23]</sup> The  $G(r)$  plots are simply a radial distribution map, where the peak positions ( $r$ ) are the real space distances between an arbitrarily chosen central carbon atom and its neighbors averaged over all atoms of the sample. As shown in Figure 4a, the first three peaks are the intra-ring distances in  $C_6$  (Figure 4b), and the first peak is the C–C bond length, 1.42 Å. The function  $g(r)$  is the ratio of the average number of atoms found at the distance of  $r$  relative to the number of atoms that would

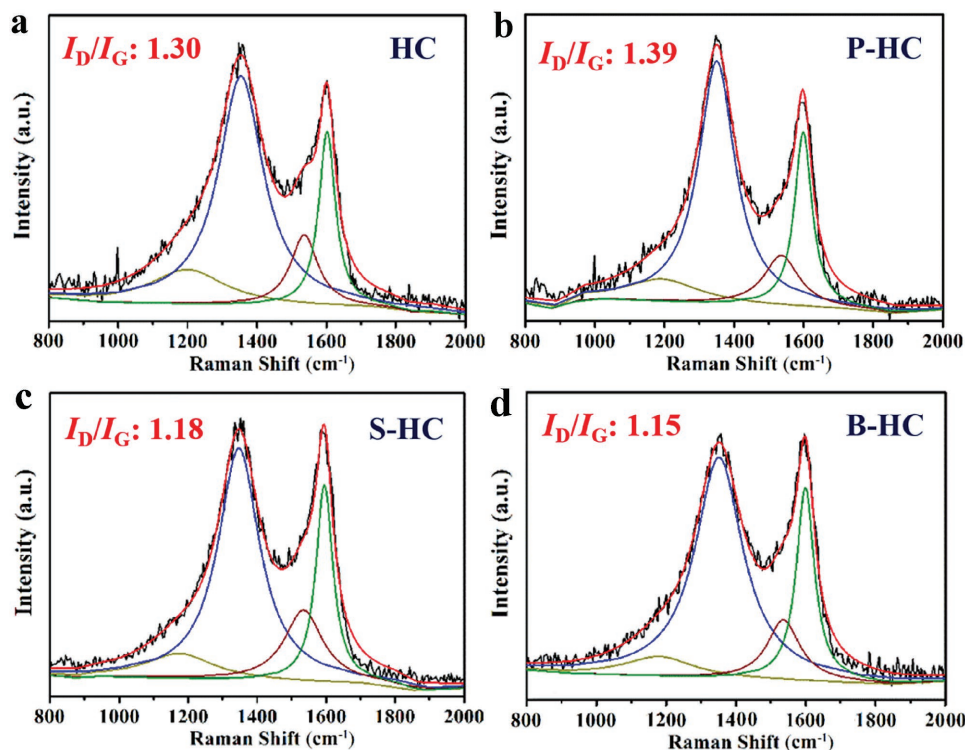


**Figure 3.** Raman spectra of different carbon samples, which are deconvoluted into four Lorentzian peaks: TPA (dark yellow), D (blue), A (wine), and G (green). a) HC, b) P-HC, c) S-HC, and d) B-HC. The results of the  $I_D/I_G$  ratios suggest that P-HC exhibits the shortest coherence length along the  $ab$  planes, where B-HC has the longest, corroborating the XRD and TEM results.

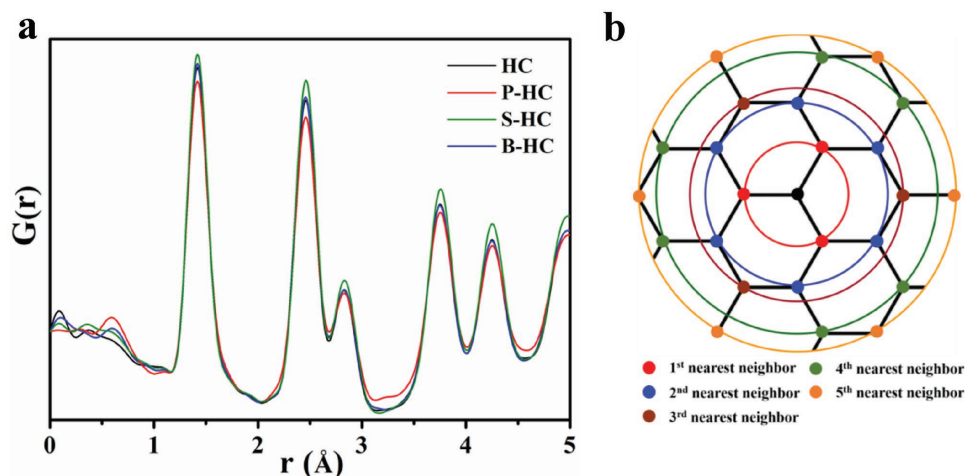


**Figure 4.** Neutron total scattering and PDF studies of carbons. a) PDF within 5 Å from neutron total scattering of HC, P-HC, B-HC, and S-HC. P-doping causes the local structure of carbon to be more defective, where S-doping slightly increases the degree of the local order. b) Schematic local structure of graphene.

be found in a completely disordered structure of the same density, and therefore, the amplitude for the first peak is related to coordination number. Boric acid ( $B^{11}$ ) was used to prepare B-HC as the absorption cross section of  $B^{11}$  is only 0.0055, comparable to 0.0035 of carbon, whereas this value is 767 for the natural mixture of boron isotopes, which would significantly damp the amplitude of the collected data. By observing the change in peaks' area upon doping, it becomes clear that heteroatom doping causes changes in peak amplitude or conversely, defect concentration. Defects include the factors that disrupt the continuum of the graphenic honey comb structure.

In PDF plots, S-HC exhibits higher amplitude of peaks than HC, which indicates less local defects. This is not surprising because  $H_2SO_4$  is a carbonization agent, which enhances the formation of  $C_6$  rings during sucrose pyrolysis. Plus, upon pyrolysis,  $H_2SO_4$  decomposes to volatile gas species, e.g.,  $SO_2$ , thus leading to a very low doping level of sulfur (0.1 wt%) in the resulting carbon. It is quite intriguing that B-HC shares the similar peak amplitude as the undoped carbon. It appears that the reduction of the boric acid precursor during boron doping does not result in more in-plane vacancies of the graphenic layers. As boron atoms can only form three bonds with the absence of strong Lewis bases, B-doping would retain well the graphenic nature of the doped carbon layers, which is consistent with the TEM and Raman results. Here, we should be cautious about the existence of in-plane doped-B and its impact on Na-ion storage. The B-doping process that does not generate more in-plane vacancies can still lead to a profound impact on its Na-ion storage properties. The doped-B sites are, in fact, in-plane defect sites as the binding energies between the doped-B and inserted Na-ions are different compared to the pristine carbon sites, which will be discussed by the DFT simulation later in the article. P-HC exhibits the lowest peak amplitude, which indicates more defects or curvatures in the local structure. Because the doped  $PO_x$  species will not be coplanar with graphenic layers, thus inducing more curvatures, as corroborated by the TEM images and the shortest coherence length  $L_a$  among all samples, as indicated by the Raman results. It is

possible that  $PO_x$  doping causes more structural vacancies as well.

To test our hypothesized Na-ion storage mechanism, we have obtained the desirable structural properties of hard carbon by heteroatom doping. First, through P- and S-doping, we have enlarged the interlayer spacing inside the turbostratic nano-domains, which should enhance the plateau capacity. Second, P- and B-doping have introduced additional structural defects inside hard carbon, where the sloping capacity should be enlarged.

## 2.2. Electrochemical Behaviors of All Carbons

Figure 5a and Table 1 provide the detailed slope/plateau capacity values, where we use the inflection point of the potential profiles to define the sloping and plateau regions: above the inflection point considered as the slope and below the point classified as the plateau. All doped carbons show quite stable cycling performance at a current density of  $20 \text{ mA g}^{-1}$ , where P-HC and S-HC exhibit a high capacity of  $327 \text{ mA h g}^{-1}$  (91% retention) and  $323 \text{ mA h g}^{-1}$  (98% retention) even after 200 cycles (Figure 5c).

When we look at the plateau capacity of electrodes during the first sodiation, both P-HC and S-HC are superior to undoped HC by exhibiting 240 and  $213 \text{ mA h g}^{-1}$  compared to  $175 \text{ mA h g}^{-1}$  of HC, and the plateau capacity for all carbon samples is relatively reversible. The capacity values confirm that a larger  $d$ -spacing due to hypervalent S- and P-doping does increase the plateau capacity. This can be well rationalized because it would be energetically more favorable for Na-ions to be inserted between more dilated graphene sheets. Note that Na-ions are, indeed, larger than the ideal size to be accommodated by the graphitic galleries, even when they are turbostratic and dilated to some degree, thus to squeeze Na-ions between carbon layers would certainly involve a penalty enthalpy change. It is this penalty enthalpy change together with the weak binding energy between the defect-free graphene layers

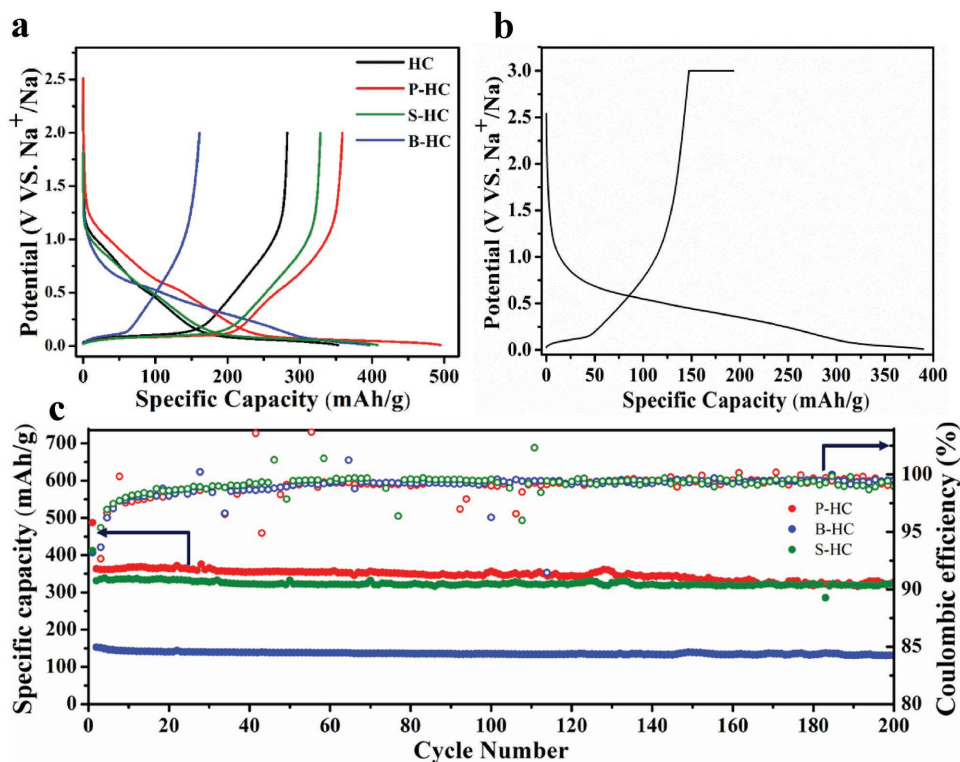


**Figure 5.** Electrochemical performance of hard carbons in C/Na half-cells. The potential is versus  $\text{Na}^+/\text{Na}$ . a) Galvanostatic sodiation/desodiation potential profiles of HC and doped hard carbons at a current rate of  $20 \text{ mA g}^{-1}$ . b) Sodiation/desodiation potential profiles of B-HC at current rate of  $20 \text{ mA g}^{-1}$  by charging it to 3.0 V and holding the potential at 3.0 V for 30 h. c) Cycling performance of doped carbons at a current density of  $20 \text{ mA g}^{-1}$ . All doped carbon materials are very stable in cycling performance.

and Na-ions (atoms) that causes the extremely low capacity of Na-ion storage by graphite. Therefore, a larger average *d*-spacing separating these graphenic layers will allow more Na-ions to be inserted before the cutoff potential of Na-plating is reached. However, it is quite interesting that B-HC exhibits an extremely small capacity from its low-potential plateau.

Looking at the sloping region during the first sodiation, B-HC and P-HC exhibit capacity values of 304 and 245  $\text{mA h g}^{-1}$ , respectively, compared to 178  $\text{mA h g}^{-1}$  of the undoped HC. Such high sloping capacity values during the first sodiation can be explained by the causality of Na/carbon defect binding for P-HC; however, it is puzzling for B-HC, because B-HC does not contain more graphenic vacancies as the PDF results revealed. Furthermore, B-HC is not likely to form a great deal of SEI due to its very modest specific surface area of  $8.0 \text{ m}^2 \text{ g}^{-1}$ . The

really shocking observation is from the first desodiation, where P-HC and B-HC generate sloping capacity values of 157 and 70  $\text{mA h g}^{-1}$ , respectively, versus 134  $\text{mA h g}^{-1}$  of HC. Both P-HC and B-HC suffer less Coulombic efficiency for the slope region: 64% and 23%, compared to 75% of HC. At this point, it is even more intriguing why B-HC's sodiation is so irreversible, as we have excluded the possibility of massive SEI formation.<sup>[14]</sup> Cyclic voltammetry (CV) results confirm the same extent of irreversible sodiation in P-HC and B-HC electrodes (Figure S3, Supporting Information). In particular, the CV curves of B-HC look completely different from the other doped and undoped hard carbon samples, where instead of exhibiting a sharp desodiation peak, the anodic scan leads to a broad bump-like peak, thus revealing the difficulty of removing Na-ions from B-HC's internal structure.

**Table 1.** Sodiation/desodiation capacities of HC and doped carbons and their capacities from plateau region and slope region.

First cycle electrode capacity [ $\text{mA h g}^{-1}$ ]	HC	P-HC	B-HC	S-HC
Total sodiation capacity	353	485	403	408
Total desodiation capacity	283	359	147	328
Sodiation capacity from plateau	175	240	99	213
Desodiation capacity from plateau	149	202	77	177
Sodiation capacity from slope	178	245	304	195
Desodiation capacity from slope	134	157	70	151

### 2.3. Computational Studies of the Na Binding

To further understand the structure–capacity correlation in hard carbon, we used DFT calculations to determine the electronic structure of sodium binding at various structural sites: idealized dopants, vacancies in contrast to ideal graphene sheet. Even though several pure computational studies on the energetics of sodium binding with doped graphene had been reported,<sup>[16,24]</sup> this article focuses on understanding of Na-ion storage in hard carbon anode, where, due to the similarity at the local atomic scale, we employ nanosheets of graphene for

the computational studies. We pay more attention on a comparative study with the expectation that the same trends in the electronic structure and energetics will carry over to the more complex misaligned, multilayered, turbostratic structures of hard carbon. Calculations were performed using the Vienna ab initio Simulation Package (VASP) using dispersion corrected exchange correlation functionals. More details about the calculations are provided in the Supporting Information. First, the binding of Na to graphene in the vicinity of B and P substitutional defects was studied. The sodiation energy was calculated using the equation

$$E_{\text{bnd}}(x) = \frac{1}{n_{\text{Na}}} (E_{\text{sub+Na}}(x) - E_{\text{sub}} - n_{\text{Na}} E_{\text{Na-BCC}}) \quad (3)$$

$$E_{\text{bnd}}(x) = \int_0^x eV(x') dx' = \int_0^{q/e} V(q') dq' \quad (4)$$

where  $E_{\text{sub+Na}}$  is the energy of the relaxed carbon substrate–Na system,  $E_{\text{sub}}$  is the energy of the carbon substrate, and  $E_{\text{Na-BCC}}$  is the per atom cohesive energy of body centered cubic (BCC) sodium metal. These calculations were performed on a  $4 \times 4$  supercell of graphene so that the dopant concentration obtained from a single substitutional defect was comparable to the experimentally measured dopant concentration. The quantity  $n_{\text{Na}}$  is the number of Na atoms in a calculation, and  $x$  is the concentration of Na to substrate atoms. Ignoring entropic contributions, the binding energy computed in this way can be related to the discharge voltage in the C/Na half-cell environment with the expression: the integral above, where  $q$  is the stored charge.

The Na atom has a positive (unfavorable) binding energy on the pristine graphene sheet, while it has a negative binding energy with both the P-doped sheet and the B-doped sheet. Utilizing a  $4 \times 4$  sheet with a single heteroatom dopant implies that the sheet formulas are  $\text{C}_{31}\text{P}$  and  $\text{C}_{31}\text{B}$ , which gives an atomic concentration percentage of 3.2% for the heteroatoms.

Though not representative of the actual hard carbon structure, the data suggest a trend that can be extrapolated to the experimental conditions. Addition of heteroatoms in the plane of the graphene leads to favorable binding energies over that

of pristine graphene, as shown in Table S1 (Supporting Information). In the case of the B-doped graphene, the increase in binding energy is much greater than that of the P-doped graphene. If we were to translate the binding energies to voltages, the sodiation voltage on a B-doped graphene sheet would be  $\approx 0.92$  V versus  $\text{Na}^+/\text{Na}$ , while the sodiation voltage for a P-doped sheet is  $\approx 0.32$  V. With these data, we conclude that, since boron acts as a p-type dopant, the system more readily accepts an electron from the sodium atom, thus leading to greater ionic interaction, and, as a result, stronger binding. Meanwhile, the phosphorous being an n-type dopant would less readily accept an electron from the sodium, thus weakening its binding energy. However, when the Bader charges for the dopant atoms are obtained, B-atom has a charge of  $\text{B}^{3+}$ , while the phosphorous has one of  $\text{P}^{3.43+}$ . This means that in both cases, three or more electrons are transferred to the neighboring carbon atoms on the graphene sheet (Figure S5, Supporting Information). As a result, there is a stronger interaction between the sodium atom and the graphene sheet in the area around the heteroatom, but not the heteroatom itself (Figure 6). Since the heteroatom is positively charged, it is expected to repel the sodium atom, which is in fact seen: the sodium atom on the phosphorous-doped graphene sheet is located 2.81 Å from the P-atom, while in the sodium atom in the boron-doped graphene sheet is located 2.57 Å from the B-atom. The lower repulsion from the boron allows the sodium atom to get closer to the negatively charged graphene sheet, thus enhancing the ionic interactions. Furthermore, the size of the P-atom causes the graphene sheet to buckle with more curvature, which is consistent with our experimental results.

Thus far, these simulations only allow us to ascertain what happens in the event that the heteroatom is bonded in-plane with the graphene sheet. However, this is not the only configuration it can take up in our system: there is the possibility of bonding at edge sites in the graphene domains, as well as the presence of oxygen and hydrogen atoms. Thus, we pushed forward and simulated those configurations as well. In the case of a heteroatom being bonded of a graphene edge, thus forming a  $\text{XC}_2$  bond, the equivalent voltage for the boron system was of 1.76 V, while it was 1.96 V for the phosphorous system

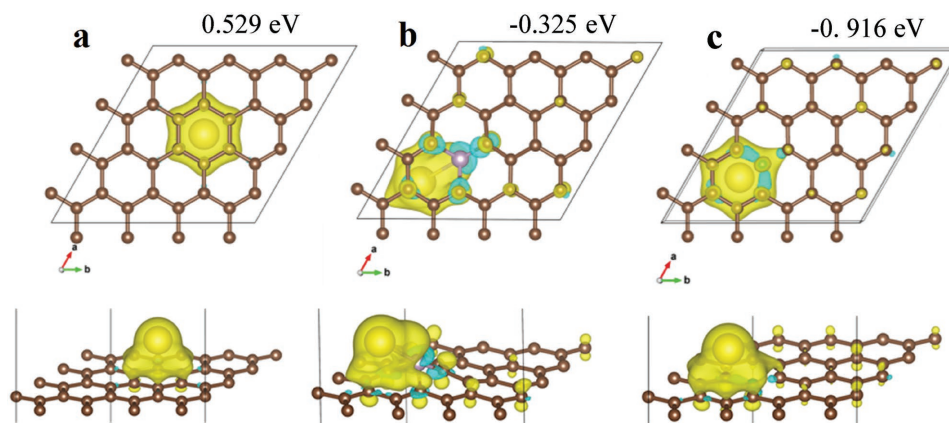


**Figure 6.** Charge distribution plots of different graphene/Na systems simulated in VASP with the binding energies of sodium ions shown. The blue regions of the charge distribution represent a negative charge, while the yellow regions represent positive charges. a) Pristine graphene, b) P-doped graphene, and c) B-doped graphene.

(Figure S6, Supporting Information). Looking at the Bader charges for the heteroatoms, the boron was found to be in a  $B^{3+}$  state, while the phosphorous was in a  $P^{2.75+}$  oxidation. This supports our previous findings that electrons are transferred from the heteroatom to the graphene system. However, in this case, as there is less degree of charge transfer on behalf of the phosphorous, the binding with the Na atom is stronger, as it is not repelled as much.

Addition of oxygen atoms to the system in various configurations was also performed, though a clear pattern in those results was harder to ascertain. In the case of the boron doping, addition of oxygen and a boron on the plane, and one on an edge site resulted in a stronger binding energies, with the increase in binding energy being more pronounced at the edge site. An oxygen atom on the in-plane boron increased the voltage to 1.37 V, while oxygen groups on the edge boron increased the voltage to 2.52 V, with that voltage being able to be increased to 3.65 V if the unit cell was shrunk to a small enough size, as to induce periodic binding (Figure S7, Supporting Information). The same configuration with oxygen atoms in the phosphorous doping yielded voltages of 1.66, 1.66, and 3.56 V with the smaller unit cell (Figure S8, Supporting Information). When looking at the Bader charges for this system, the boron stayed at  $B^{3+}$ , while the phosphorous was at  $P^{5+}$ .

Since the oxidation P(II) was heavily featured in the XPS data, but the oxidation due to the addition of oxygen was entirely suggestive of P(V) oxidation, we performed additional simulation with OH groups, with the thought that the H would suppress the electron withdrawing tendencies of the oxygen functional group on the phosphorous. Converged simulations show charges of  $P^{2.64+}$  and  $P^{3.37+}$  with voltages of 2.62 and 2.69 V, respectively (Figure S9, Supporting Information). It also must be noted that both the phosphorous atoms were present at edge sites on the graphene sheet. Aside from the increased voltage in Na atom binding, these simulations also show that, while not the P(II) illustrated in the XPS results, the addition of H to carbonyl groups attenuates their electron withdrawing power.

Overall, there are a few takeaways from these simulations in helping us better understand the impact of heteroatom in

addition to graphene structures. First, the heteroatoms act as electron donors to the graphene sheet, while themselves acting at positive charges. This leads to stronger ionic bonding between the sodium atom and the graphene sheet, and is the strongest in boron. Additionally, the presence of oxygen in the system also increases the overall voltage of the sodium atom storage.

Correlating the simulation data to the first-cycle sodiation profiles of the B-HC and P-HC, we see a lot of similarities: the B-HC profile has a much more pronounced slope, and on average has a much higher voltage than the P-HC profile. Considering that Na atoms bind more strongly, and thus at higher voltages, to boron heteroatom, along with the fact that B-HC also had a higher oxygen concentration, which is also associated with higher voltages, such profiles match up well with the DFT results, and help to explain why the B-HC has a much longer slope than the P-HC.

Though helpful, these initial results are to be taken with caution, as they make the assumption that the heteroatoms are only bonded with carbon atoms. However, there is another structural feature of the carbon material whose effect on Na-ion storage we can also evaluate: the presence of vacancies. From the PDF results, we know that P-HC is of a higher defect concentration than HC. When simulating a monovacancy, divacancy, and a large-vacancy defect, where we define them all as in-plane defects, we see that the binding energy is very favorable, especially in the base of the large-vacancy defect (Table S2, Supporting Information). From the charge density plots (Figure 7), we see that negative charges gather at defect  $sp^2$  sites, thereby acting as favorable binding locations for Na atoms. This is especially true in the case of the monovacancy defect and the large-vacancy defect, which show strong regions of charge at  $sp$ -bonded carbons, which are highly favorable for binding with Na atoms. This may explain why with more defects P-HC exhibits an enhanced presence of sloping capacity. Cohn et al. recently reported the function of carbon nanoparticles coated on metal current collector as nucleation sites for Na-metal plating.<sup>[25]</sup> The evenly distributed doping sites and their higher binding energy with sodium ions would reduce

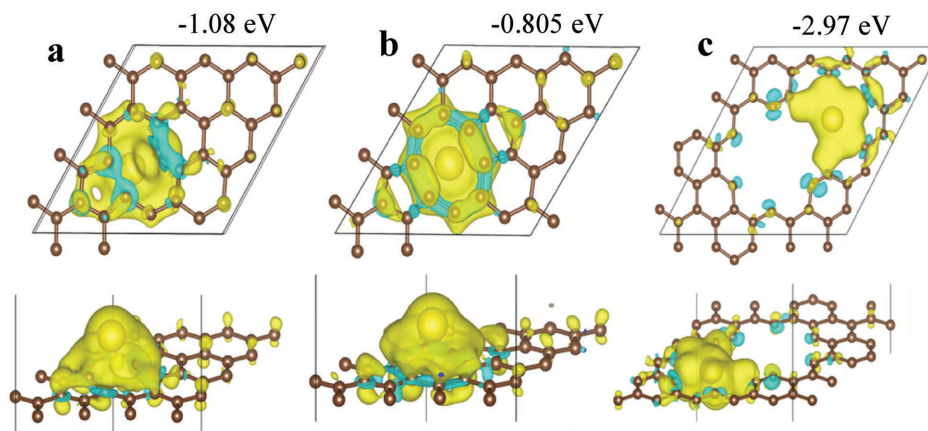


**Figure 7.** Charge distribution plots of different graphene/Na systems simulated in VASP with the binding energies of sodium ions shown. The blue regions of the charge distribution represent a negative charge, while the yellow regions represent positive charges. a) Monovacancy graphene, b) divacancy graphene, and c) a large in-plane defect. With both monovacancy and divacancy, the Na-ion hovers on the surface of graphene layer whereas in the case of the large vacancy, Na-ion is cuddled in the void.

the sodium plating barrier and decrease the overpotential. This high reversible capacity and good cycling performance of P-HC and S-HC suggest that these doped carbons are very promising to be used as a carbon nucleation layer for sodium plating.

Note that different dopants indeed have various numbers of doping sites; however, it is clear that different identities of dopants generate a stark contrast in their impacts on the Na-ion storage performance of hard carbon anodes. Such impacts may come from the changed carbon structures, that is, with more vacancy defects, or from the dopant themselves as heteroatom defects. For example, in terms of the sloping region, P-doping introduces more carbon vacancy defects to graphenic layers, as revealed by neutron total scattering/PDF, which rationalizes its higher sloping capacity; however, B-doping does not cause more carbon vacancy defects, according to Raman and PDF results, but B-HC exhibits the highest sloping capacity in its first sodiation. This can only be understood by the fact that the doped boron atoms themselves are strong Na-binding “defects,” as revealed by DFT studies, and the binding energy between the doped B sites and Na-ions are comparable to binding with carbon vacancy sites. This explains why both P-HC and B-HC show higher sloping capacity than undoped HC, where the trend is that sites with higher binding energy values would contribute to the sloping capacity.

Here, we attempt to explain the poor reversibility of B-HC during the first cycle. First, B-HC exhibits a very limited low-potential plateau capacity of 99 out of 403 mA h g<sup>-1</sup> for the overall sodiation. This is in sharp contrast to 175, 240, and 213 mA h g<sup>-1</sup> for HC, P-HC, and S-HC. When scrutinizing the TEM imaging results, one cannot easily differentiate that of B-HC from the TEM images of other carbons because they all contain turbostratic stacking of curved graphenic layers. Considering its very large sodiation capacity of 403 mA h g<sup>-1</sup> and an expected minimal SEI formation due to the low specific surface area, “intercalation” of Na-ions must have taken place between the B-doped graphenic layers during the first sodiation. Considering the high binding energy between the doped B and the inserted Na-ions, we hypothesize that the normally low-potential plateau for other carbon samples is replaced by the high-binding-energy “intercalation” in B-HC. However, this high-binding-energy intercalation traps Na-ions, causing the high irreversible capacity in the first cycle. The basic rationale for such trapping is that the motion of Na-ions through the “sticky” bilayers in the turbostratic domains becomes very restricted due to the high binding energy, which traps the Na ions.

To prove the irreversibility is of the energetic causality, we apply a large voltage bias on the C/Na half-cells to see whether a larger extent of desodiation can be forced to take place. When the half-cell was held at a constant voltage of 3.0 V for 30 h, an additional capacity of 40 mA h g<sup>-1</sup> was recovered (Figure 5b). It is expected that applying an even higher cell voltage can extract more desodiation capacity. This suggests that the B-HC anode can reversibly store Na atoms, but it does so very strongly. Thus, simply desodiating the anode up to a cut-off potential of 2.0 V is not sufficiently high to fully remove all of the inserted Na atoms. This behavior is consistent with the high binding energies from the in-plane boron in turbostratic domains.

### 3. Conclusion

In conclusion, via well-controlled syntheses, comprehensive structural characterization and first principles DFT studies, we provide in-depth insights on the correlation between the local structure of hard carbon, and the corresponding capacity performance. We confirm the linkage between high-energy binding with Na-ions and the sloping region of potential profiles, particularly for the first sodiation. We also confirm the favorable impacts of larger interlayer spacing between graphenic sheets on extending the sodium storage capacity from the low-potential plateau. We employed B-doping to elucidate that high-energy in-plane “defect” sites inside turbostratic nanodomains can cause a large irreversible capacity in the first cycle. It means that albeit B-doping does not generate more in-plane carbon vacancies, if there existed in-plane vacancies in other hard carbon materials that bind Na-ion strongly, it will affect the first-cycle reversibility as well. Overall, we elucidate the Na-ion storage mechanism for hard carbon as an NIB anode, and we provide the design principle as such that the ideal hard carbon anode should be a low surface area ensemble of dilated turbostratic nanodomains with more curvatures or more non-in-plane high-energy defects. We believe that these fundamental insights into Na-ion storage mechanisms will guide community to steer the development and optimization of hard carbon anodes and as such will hasten commercialization of high capacity Na-ion batteries.

### 4. Experimental Section

**Materials Synthesis:** Modified Hummer’s method was applied to prepare aqueous GO suspension. In a typical experiment, 2 g sucrose was added to GO suspension (1.8 mg mL<sup>-1</sup>) with a mass ratio of 80:1. Then, an oxo-acid precursor, H<sub>3</sub>PO<sub>4</sub>, or H<sub>2</sub>SO<sub>4</sub> or H<sub>3</sub>BO<sub>3</sub> was added to the suspension with a designed mass ratio of the corresponding dopant of 5 wt% for P-HC, S-HC, and B-HC. Undoped hard carbon suspension was prepared with the same method without adding a dopant precursor. The obtained suspension was dried at 80 °C for 48 h, dehydrated at 180 °C for 24 h, and then pyrolyzed at 1100 °C for 5 h under Ar flow.

**Materials Characterization:** The doping levels of all doped carbon were measured by ICP-OES. The density of all carbons was measured by a density measurement kit using cyclohexane as the solvent. N<sub>2</sub> sorption measurements were performed on a Micromeritics TriStar II 3020 analyzer for BET surface area. XPS measurements were performed in a Physical Electronics Quanterra Scanning ESCA Microprobe with a focused monochromatic Al K $\alpha$  X-ray (1486.6 eV) source for excitation. The X-ray beam used was a 25 W, 100  $\mu$ m X-ray beam spot at the sample. High-resolution SEM was performed on FEI NOVA 230 to obtain the morphology of all carbons. TEM images were recorded by a FEI Titan 80-200 TEM. The XRD patterns of obtained materials were collected on a Rigaku Ultima IV Diffractometer with Cu K $\alpha$  ( $\lambda$  = 1.5406 Å) radiation and the patterns were fitted with the PDXL software. WITec confocal Raman spectrometer with a 514 nm laser source was used to gather Raman spectra and the spectra were fitted by Origin 8.5. Neutron total scattering data were collected at the Nanoscale Ordered Materials Diffractometer (NOMAD), Spallation Neutron Source, at Oak Ridge National Laboratory. Samples were loaded into quartz capillaries for analysis.

**Electrochemical Measurements:** All the electrochemical measurements were done with coin cells (CR2032). The electrodes were composed of active materials, polyvinylidene fluoride (PVdF), and carbon black with a mass ratio of 80:10:10. All these components were mixed together

in a mortar and grounded in N-methyl-2-pyrrolidone (NMP), and the obtained slurry was coated onto Al foil by doctor blade and dried at 100 °C for 12 h under vacuum. The active mass loading for all electrodes are between 1.5 and 2 mg cm<sup>-2</sup>. The counter/reference electrode was sodium metal and the electrolyte was 1.0 mol L<sup>-1</sup> NaPF<sub>6</sub> solution in ethylene carbonate (EC)/diethyl carbonate (DEC) (1:1 in volume). Arbin BT2000 system was used to test galvanostatic sodiation/desodiation in the potential range of 0.01–2 V versus Na<sup>+</sup>/Na under room temperature.

## Supporting Information

Supporting Information is available from the Wiley Online Library or from the author.

## Acknowledgements

Z.L. and C.B. contributed equally to this work. X.J., P.A.G., and M.D. thank the financial supports from the National Science Foundation of the United States, Award No. 1507391. The authors are thankful to Prof. Chih-Hung Chang and Mr. Changqing Pan for Raman analysis. The authors thank the help of Mr. Andy Ungerer and Mr. Jesse Muratli on ICP-OES measurements and ICP sample preparation. This research used resources at the Spallation Neutron Source, a DOE Office of Science User Facility operated by Oak Ridge National Laboratory. This is based upon work supported by the U.S. Department of Energy, Office of Science, under Contract No. DE-AC05-00OR22725.

## Conflict of Interest

The authors declare no conflict of interest.

## Keywords

hard carbon anodes, heteroatom doping, local structures, mechanisms, Na-ion batteries

Received: December 26, 2016

Revised: March 19, 2017

Published online:

- [1] a) Y. Xu, Q. Wei, C. Xu, Q. Li, Q. An, P. Zhang, J. Sheng, L. Zhou, L. Mai, *Adv. Energy Mater.* **2016**, *6*, 1600389; b) Y. Fang, L. Xiao, X. Ai, Y. Cao, H. Yang, *Adv. Mater.* **2015**, *27*, 5895; c) L. Mu, S. Xu, Y. Li, Y. S. Hu, H. Li, L. Chen, X. Huang, *Adv. Mater.* **2015**, *27*, 6928; d) M. Sathiyaa, K. Hemalatha, K. Ramesha, J.-M. Tarascon, A. Prakash, *Chem. Mater.* **2012**, *24*, 1846; e) Z. Jian, L. Zhao, H. Pan, Y.-S. Hu, H. Li, W. Chen, L. Chen, *Electrochem. Commun.* **2012**, *14*, 86.
- [2] a) B. Jache, P. Adelhelm, *Angew. Chem., Int. Ed.* **2014**, *53*, 10169; b) Y. Wen, K. He, Y. Zhu, F. Han, Y. Xu, I. Matsuda, Y. Ishii, J. Cumings, C. Wang, *Nat. Commun.* **2014**, *5*, 4033.
- [3] R. E. Franklin, *Proc. R. Soc. London, Ser. A* **1951**, *209*, 196.
- [4] D. Stevens, J. Dahn, *J. Electrochem. Soc.* **2000**, *147*, 1271.
- [5] Z. Li, L. Ma, T. W. Surta, C. Bommier, Z. Jian, Z. Xing, W. F. Stickle, M. Dolgos, K. Amine, J. Lu, *ACS Energy Lett.* **2016**, *1*, 395.
- [6] J. Ding, H. Wang, Z. Li, A. Kohandehghan, K. Cui, Z. Xu, B. Zahiri, X. Tan, E. M. Lotfabad, B. C. Olsen, *ACS Nano* **2013**, *7*, 11004.
- [7] Y. Li, Y. S. Hu, M. M. Titirici, L. Chen, X. Huang, *Adv. Energy Mater.* **2016**, *6*, 1600659.
- [8] F. Shen, W. Luo, J. Dai, Y. Yao, M. Zhu, E. Hitz, Y. Tang, Y. Chen, V. L. Sprenkle, X. Li, L. Hu, *Adv. Energy Mater.* **2016**, *6*, 1600377.
- [9] E. M. Lotfabad, J. Ding, K. Cui, A. Kohandehghan, W. P. Kalisvaart, M. Hazelton, D. Mitlin, *ACS Nano* **2014**, *8*, 7115.
- [10] C. Bommier, T. W. Surta, M. Dolgos, X. Ji, *Nano Lett.* **2015**, *15*, 5888.
- [11] S. Komaba, W. Murata, T. Ishikawa, N. Yabuuchi, T. Ozeki, T. Nakayama, A. Ogata, K. Gotoh, K. Fujiwara, *Adv. Funct. Mater.* **2011**, *21*, 3859.
- [12] a) L. Qie, W. Chen, X. Xiong, C. Hu, F. Zou, P. Hu, Y. Huang, *Adv. Sci.* **2015**, *2*, 1500195; b) W. Li, M. Zhou, H. Li, K. Wang, S. Cheng, K. Jiang, *Energy Environ. Sci.* **2015**, *8*, 2916.
- [13] a) F. Yang, Z. Zhang, K. Du, X. Zhao, W. Chen, Y. Lai, J. Li, *Carbon* **2015**, *91*, 88; b) P. Wang, B. Qiao, Y. Du, Y. Li, X. Zhou, Z. Dai, J. Bao, *J. Phys. Chem. C* **2015**, *119*, 21336; c) D. Xu, C. Chen, J. Xie, B. Zhang, L. Miao, J. Cai, Y. Huang, L. Zhang, *Adv. Energy Mater.* **2016**, *6*, 1501929; d) Y. Li, Z. Wang, L. Li, S. Peng, L. Zhang, M. Srinivasan, S. Ramakrishna, *Carbon* **2016**, *99*, 556; e) B. Ruan, J. Wang, D. Shi, Y. Xu, S. Chou, H. Liu, J. Wang, *J. Mater. Chem. A* **2015**, *3*, 19011; f) J. Zhu, C. Chen, Y. Lu, Y. Ge, H. Jiang, K. Fu, X. Zhang, *Carbon* **2015**, *94*, 189; g) T. Yang, T. Qian, M. Wang, X. Shen, N. Xu, Z. Sun, C. Yan, *Adv. Mater.* **2016**, *28*, 539; h) H. Hou, L. Shao, Y. Zhang, G. Zou, J. Chen, X. Ji, *Adv. Sci.* **2016**, *3*, 1600243.
- [14] C. Bommier, W. Luo, W.-Y. Gao, A. Greaney, S. Ma, X. Ji, *Carbon* **2014**, *76*, 165.
- [15] W. Luo, C. Bommier, Z. Jian, X. Li, R. Carter, S. Vail, Y. Lu, J.-J. Lee, X. Ji, *ACS Appl. Mater. Interfaces* **2015**, *7*, 2626.
- [16] C. Ling, F. Mizuno, *Phys. Chem. Chem. Phys.* **2014**, *16*, 10419.
- [17] J. M. Stratford, P. K. Allan, O. Pecher, P. A. Chater, C. P. Grey, *Chem. Commun.* **2016**, *52*, 12430.
- [18] a) J. Zhang, L. Qu, G. Shi, J. Liu, J. Chen, L. Dai, *Angew. Chem.* **2015**, *128*, 2270; b) X. Yan, Y. Liu, X. Fan, X. Jia, Y. Yu, X. Yang, *J. Power Sources* **2014**, *248*, 745.
- [19] Y. Yan, Y.-X. Yin, S. Xin, Y.-G. Guo, L.-J. Wan, *Chem. Commun.* **2012**, *48*, 10663.
- [20] M. Enterría, M. Pereira, J. Martins, J. Figueiredo, *Carbon* **2015**, *95*, 72.
- [21] L. Cancado, K. Takai, T. Enoki, M. Endo, Y. Kim, H. Mizusaki, A. Jorio, L. Coelho, R. Magalhaes-Paniago, M. Pimenta, *Appl. Phys. Lett.* **2006**, *88*, 163106.
- [22] a) V. Petkov, R. DiFrancesco, S. Billinge, M. Acharya, H. Foley, *Philos. Mag. B* **1999**, *79*, 1519; b) S. Chatterjee, E. B. Jones, A. C. Clingenpeel, A. M. McKenna, O. Rios, N. W. McNutt, D. J. Keffer, A. Johs, *ACS Sustainable Chem. Eng.* **2014**, *2*, 2002; c) C. Shi, E. L. Redmond, A. Mazaheripour, P. Juhas, T. F. Fuller, S. J. Billinge, *J. Phys. Chem. C* **2013**, *117*, 7226.
- [23] W. Drnowski, C. I. Contescu, A. Llobet, N. C. Gallego, T. Egami, *J. Phys. Chem. C* **2012**, *116*, 2946.
- [24] a) L. Yao, W. Cao, M. Cao, *Curr. Appl. Phys.* **2016**, *16*, 574; b) Y. J. Kang, S. C. Jung, J. W. Choi, Y. K. Han, *Chem. Mater.* **2015**, *27*, 5402.
- [25] A. P. Cohn, N. Muralidharan, R. Carter, K. Share, C. L. Pint, *Nano Lett.* **2012**, *17*, 1296.